

3D-OOCS: Learning Prostate Segmentation with Inductive Bias

Shrajan Bhandary¹, Zahra Babaiee¹, Dejan Kostyszyn², Tobias Fechter², Constantinos Zamboglou², Anca Grosu², Radu Grosu¹

¹ Technische Universität Wien Vienna, Austria

² Department of Radiation Oncology, University Medical Centre Freiburg

shrajan.bhandary@tuwien.ac.at, zahra.babaiee@tuwien.ac.at, dejan.kostyszyn@uniklinik-freiburg.de, tobias.fechter@uniklinik-freiburg.de, constantinos.zamboglou@uniklinik-freiburg.de, anca.grosu@uniklinik-freiburg.de, radu.grosu@tuwien.ac.at

Abstract

Despite the great success of convolutional neural networks (CNN) in 3D medical image segmentation tasks, the methods currently in use are still not robust enough to the different protocols utilized by different scanners, and to the variety of image properties or artefacts they produce. To this end, we introduce OOCS-enhanced networks, a novel architecture inspired by the innate nature of visual processing in the vertebrates. With different 3D U-Net variants as the base, we add two 3D residual components to the second encoder blocks: on and off center-surround (OOCS). They generalise the ganglion pathways in the retina to a 3D setting. The use of 2D-OOCS in any standard CNN network complements the feedforward framework with sharp edge-detection inductive biases. The use of 3D-OOCS also helps 3D U-Nets to scrutinise and delineate anatomical structures present in 3D images with increased accuracy. We compared the state-of-the-art 3D U-Nets with their 3D-OOCS extensions and showed the superior accuracy and robustness of the latter in automatic prostate segmentation from 3D Magnetic Resonance Images (MRIs). For a fair comparison, we trained and tested all the investigated 3D U-Nets with the same pipeline, including automatic hyperparameter optimisation and data augmentation.

Introduction

Prostate cancer (PCa) is one of the leading causes of death in males. It is presumed that one in eight men will be diagnosed with it during his lifetime (AmericanCancerSociety 2021). Radiation therapy (RT) is one of the main options of medical care, but as with most treatments, it has its drawbacks. Moreover, due to the unique traits of different patients, there is an urgent need to personalize and improve it. Personalization can be achieved by considering the individual PCa biology and the disease process of each patient. Quality improvement can be accomplished by increasing the robustness of prostate segmentation, in addition to that of intraprostatic gross-tumour-volume (GTV) segmentation (Spohn et al. 2021). Both are important for a variety of applications, such as prostate-volume measurement, targeted biopsies, pre-radiation treatment planning, and monitoring disease progression over time (Goldenberg, Nir, and Salcudean 2019). However, manual segmentation of structures in the pelvic region by physicians, based on medi-

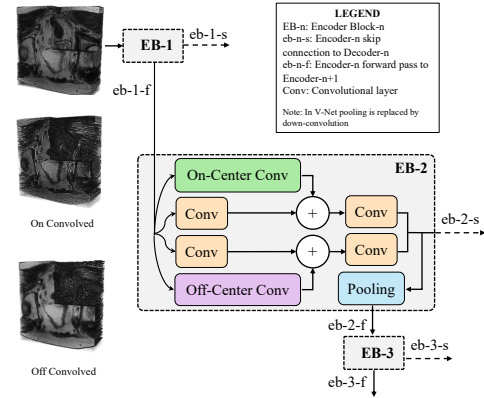


Figure 1: Extending U-Net-like architectures with the two 3D-OOCS inductive biases enhances their segmentation performance and their robustness to distribution shifts.

cal images, underlies significant interobserver heterogeneity and is time consuming (Steenbergen et al. 2015; Rischke et al. 2013).

Since the success of AlexNet (Krizhevsky, Sutskever, and Hinton 2012), the biomedical-imaging community has investigated various CNN architectures as promising solutions to enhancing cancer-detection efficiency (Singh et al. 2020). To facilitate early PCa detection, deep learning (DL) CNN-based approaches could be thus pivotal in improving automatic prostate and GTV segmentation. Semantic segmentation, converting raw image data into meaningful and structured information, plays a crucial role in discerning MRI images. Automatic segmentation can be deployed in various clinical applications, such as the diagnosis, prognosis, and treatment of prostate cancer (Goldenberg, Nir, and Salcudean 2019; Singh et al. 2020).

Even though DL-based networks have achieved tremendous breakthroughs in biomedical organ or lesion segmentation scenarios in recent years, their capabilities are limited. In particular, there is a scarcity of robust algorithms that can carry out automatic prostate and PCa lesion segmentation. This limitation stems from several factors, such as lack of publicly available standard data, steep learning curves, the requirement of experience in area-specific tasks etc (Isensee et al. 2021). Furthermore, 3D biomed-

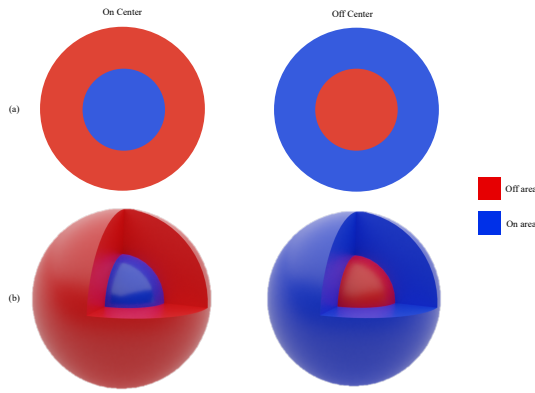


Figure 2: On (left) and Off (right) Center-Surround receptive fields. a) For the 2-D case. b) For the 3-D case.

ical image-segmentation scenarios vary in dataset properties, like imaging modality, image sizes, voxel spacings, and class-imbalance ratios. Training a network with these datasets can have adverse artifacts if they are not pre-processed appropriately. Learning from limited data is of even more importance in tasks with 3D medical images, because to our knowledge, pre-trained networks on large-scale natural image datasets do not exist. Moreover, networks developed for 2D scenarios cannot be used directly for 3D images (Litjens et al. 2017). Therefore, the first essential step in overcoming this issue would be to make the algorithms capable of automatic segmentation of medical images more robust.

Much work in recent years has tried to enhance the performance of CNNs with biologically inspired architectures. The retina is one of the primary sources of inspiration from the visual system. As the first processor of images, the retina plays a vital role in extracting low-level features such as object edges (Kandel et al. 2013). The ganglion neurons are the last layer of cells in the retina, transmitting the neural images to the brain. There are two types of neurons in the retina: On and Off. They act in parallel pathways and receive unique and complementary features (Callaway 2005; Zaghoul, Boahen, and Demb 2003; Shapley and Perry 1986). The receptive fields of On ganglion neurons have a center-surround structure, with an excitatory center and inhibitory surround. The opposite holds for Off neurons (Kuffler 1953; Kandel et al. 2013; Enroth-Cugell and Pinto 1972). This On-Off Center-Surround (OOCS) structure helps carry out a very accurate edge detection in the retina, which is particularly important in image segmentation.

The receptive fields in the retina are two dimensional, as the retina captures 2D images. The 3D perception, or the depth perception, is merely a brain trick performed by combining binocular images (Kandel et al. 2013). In 3D CNNs, a three-dimensional filter convolves the images in 3 axes (x , y , z) (Tran et al. 2015). To introduce OOCS receptive-fields to 3D CNNs, we extend them to 3D, beyond what exists in the retina. While in 2D receptive fields consist of a circular center and a concentric region around, in 3D they consist of a spherical center and a concentric surround. Figure 2 shows

the 2D and 3D models of OOCS receptive fields.

U-Nets are a particular type of CNNs that were originally designed to work with small datasets and yield a highly accurate segmentation (Ronneberger, Fischer, and Brox 2015), first in 2D and later on in 3D medical imaging scenarios (Çiçek et al. 2016). The U-Net network has an encoder-decoder structure, where the encoder performs as a classification network based on annotated images. In contrast, the decoder is (loosely) a dual network that reconstructs the image from its discriminative features (low-dimensional feature space) in the original pixel-level space (high-dimensional features). Several works in recent years have investigated other U-Net based configurations and achieved state-of-the-art performances, such as networks with residual connections, attention mechanisms, and strided convolutions (Zhou et al. 2018; Oktay et al. 2018; Milletari, Navab, and Ahmadi 2016).

A survey conducted on the application of various DL approaches in medical image analysis revealed that the exact architecture of the network is not the most crucial factor in obtaining good results (Litjens et al. 2017). While participating in challenges, even though different competitors conducted their experiments with the same architecture, using the same datasets, they witnessed varying results. The critical aspect showcased by the winners was their deep knowledge of the task at hand that further led to the development of novel data pre-processing and augmentation techniques and training strategies. Furthermore, DL algorithms that can appropriately capture the receptive field required to carry out the task also perform well. Lastly, the performance could also be boosted by optimizing the hyperparameters of the network (Isensee et al. 2021; Litjens et al. 2017).

Inspired by the OOCS retinal circuitry and motivated by the significant efficacy of 2D OOCS in image-classification tasks (Babaiee et al. 2021), we investigated if the 3D OOCS extension can improve the accuracy and robustness of U-Net-like architectures. We first designed the 3D OOCS kernels and then modified the second encoder block of our U-Net baselines, with On and Off parallel pathways. Our experiments on prostate segmentation show that introducing OOCS blocks to a U-Net-like network not only improves its performance but also increases the network’s robustness to test-set distribution shifts, such as noise, blurring, and motion. Since hyper-parameter optimization plays a vital role in the results obtained by a network (Isensee et al. 2021), in our comparison, we carefully tuned the hyper-parameters for all the networks in the same way.

Summary of Contributions:

- *3D-OOCS Kernels.* We extend the 2D OOCS inductive biases of the retina, to a 3D medical-image setting.
- *3D-OOCS Encoders.* We use these biases to develop 3D OOCS encoder blocks, for U-Net like architectures.
- *Hyper-Parameter Tuning.* We develop a fair setting for hyper-parameter tuning of baselines and their extensions.
- *Experimental Evaluation.* We show improved prostate-segmentation accuracy and robustness in our extensions.

Related Work

Medical-Image Segmentation

Prostate-Gland Segmentation In the past decade, significant research has been devoted to the automatic prostate-segmentation from MRIs (Gillespie et al. 2020). A CNN and training strategy based on statistical shape models was developed for the prostate segmentation in MRI (Karimi et al. 2018). The strategy utilized a dataset with T2-weighted axial images, in which a radiologist manually labeled the prostate. To overcome the challenge of insufficient training data, the subtle modes of variation in prostate shapes were learned in a process known as statistical shape modelling. Furthermore, synthetic images were generated to expand the training set, provided these examples were plausible representations of the actual data through translation, rotation, mirroring, or deformation. This method utilized an overlap function, called Dice-Sørensen Coefficient (DSC), to determine the model’s performance. A similar statistical shape model based on MRI was used to improve the segmentation of the prostate in transrectal ultrasonography (TRUS) volume determinations (Zeng et al. 2018). The authors of (Lei et al. 2020) introduced a CNN architecture that first created synthetic magnetic resonance images (sMRI) with a cycle generative adversarial network from CT images. Secondly, the sMRIs were utilized by a deep attention fully convolution network (DAFCN) to segment prostate contours.

Currently, the two most widely used and publicly available prostate-contour annotated datasets are the Prostate MR Image Segmentation (PROMISE) 2012 challenge (Litjens et al. 2014), and the Medical Segmentation Decathlon (MSD)(Simpson et al. 2019). A framework called nnU-Net (‘no-new-Net’) was created that provides robust, and self-adapting networks based on 2D and 3D vanilla U-Nets, as well as a U-Net cascade (Isensee et al. 2019). The nnU-Net used the 3D MR images from both the PROMISE-12 and the MSD challenges in the prostate-contour segmentation tasks. A graph convolutional network was used to create an interactive segmentation method based on the automatically prostate-gland from the PROMISE-12 dataset (Tian et al. 2020).

U-Net Variations U-Nets are one of the most popular biomedical-segmentation architectures, used as the backbone of numerous networks, many of which propose extensions and advances (Isensee et al. 2021). However, these networks were developed for individual needs, lack sufficient documentation, and often produce sub-optimal pipeline configurations that are difficult to replicate. That being said, a few novel ideas have been put forth. One such being the attention U-Net (Oktay et al. 2018), where the authors found that by employing the attention-gate (AG) module in the U-Net, the network automatically learns to emphasize target structures of varying shapes and sizes. This network was trained and evaluated using two separate abdominal 3D CT scans, focusing on segmenting pancreatic boundaries. The attention U-Net performed better than the 3D U-Net, by highlighting the essential features and effectively suppressing the irrelevant regions in the images.

Another popular volumetric-segmentation architecture, called the V-Net, replaces pooling layers with down/up convolutions so that there is a smaller memory footprint during training (Milletari, Navab, and Ahmadi 2016). It also uses skip connections within every encoder block to learn residual functions, which also helps to expedite network convergence. The V-Net was trained on 50 MRI volumes (with their respective ground truth annotations), acquired from the PROMISE-2012 challenge.

Biologically Inspired Architectures

Vision models. Originally, they were inspired by neuroscience and psychology. In the meantime, both neuroscience and artificial intelligence (AI), in particular computer vision, have enormously progressed. Nevertheless, most of today’s neural networks remained only loosely inspired by the visual system. The interaction between the fields has become less common, compared to the early age of AI, despite the importance of neuroscience in generating accelerating ideas for AI (Brooks et al. 2012; Hassabis et al. 2017).

While the close engagement of AI with neuroscience declined, there are still many recent developments, which have been inspired by biology. In particular, there has been considerable attention to seeking neuroscience-inspired CNN architectures and enhancements, and several efforts on increasing the robustness of CNNs, by incorporating biological attributes into them (Nayebi and Ganguli 2017; Li et al. 2019; Dapello et al. 2020; Babaiee et al. 2021).

2D OOCs kernels. A recent paper introduced OOCs parallel pathways to CNNs and evaluated their effect in several image-classification and robustness scenarios (Babaiee et al. 2021). OOCs-CNNs outperformed the CNNs baselines in accuracy and surpassed state-of-the-art regularisation methods in unseen lighting conditions and noisy test sets (Babaiee et al. 2021). However, that paper only studied OOCs for image classification tasks and was limited to 2-dimensional natural image datasets. In this paper, we investigate 3D OOCs, which are beyond what exists in the human visual system. We also show the superior performance of networks incorporating 3D OOCs compared to their U-Net-like baselines in the 3D prostate segmentation task. Our experiments show that similar to the 2D version, 3D OOCs extensions significantly enhance accuracy and robustness.

Method

In this section we first show how we compute the 3D OOCs kernels. We then discuss how to extend a U-Net-like architecture with OOCs inductive biases.

3D OOCs Kernels

OOCs receptive fields are captured with a difference of two Gaussians (DoG) (Rodieck 1965). For 2D kernels, Equation (1) computes their center and surround weights (Petkov and Visser 2005; Kruizinga and Petkov 2000):

$$DoG_{\sigma,\gamma}(x,y) = \frac{A_c}{\gamma^2} e^{-\frac{x^2+y^2}{2\gamma^2\sigma^2}} - A_s e^{-\frac{x^2+y^2}{2\sigma^2}} \quad (1)$$

In Equation (1), γ is the ratio of the radius of the center to the surround, $\gamma < 1$, σ is the variance of the Gaussian function, and A_c and A_s are the center and surround coefficients.

To construct 3D-OOCS kernels, the naive way would be to use Equation (1), and repeat the kernels in the third axis. However, this approach would result in a cylindrical center-surround structure, instead of a spherical one, with excitatory center, and an inhibitory surround. We therefore use a 3D DoG, with three parameters, extending the 2D version:

$$DoG_{\sigma,\gamma}(x, y, z) = \frac{A_c}{\gamma^3} e^{-\frac{x^2+y^2+z^2}{2\gamma^2\sigma^2}} - A_s e^{-\frac{x^2+y^2+z^2}{2\sigma^2}} \quad (2)$$

We set the absolute value of the sum of the negative and positive weights, to be equal to an arbitrary value $c \geq 1$. This ensures the proper balance between excitation and inhibition and the kernel weights will be large enough.

$$\iiint [DoG_{\sigma,\gamma}(x, y, z)]^+ dx dy dz = c, \quad (3)$$

$$\iiint [DoG_{\sigma,\gamma}(x, y, z)]^- dx dy dz = -c \quad (4)$$

By setting the sum of negative and positive values to be equal, the coefficients A_c and A_s will be equal in the infinite continuous case. To show this, we can write the DoG equation in polar coordinates:

$$\int_0^{r_s} \int_0^\pi \int_0^{2\pi} r^2 \sin(\varphi) \left(\frac{A_c}{\gamma^3} e^{-\frac{r^2}{2\gamma^2\sigma^2}} - A_s e^{-\frac{r^2}{2\sigma^2}} \right) d\theta d\varphi dr \quad (5)$$

Here r is the radius of the central sphere. We can calculate the integral when $r \rightarrow \infty$, and by knowing the sum of positive and negative weights equals to zero, we have:

$$\frac{2\sqrt{2}\pi^{\frac{3}{2}}}{\left(\frac{1}{\sigma^2}\right)^{\frac{3}{2}}} (A_c - A_s) = 0 \Rightarrow A_c = A_s \quad (6)$$

Assuming that the values of the coefficients are still close enough in the finite discrete case as well, we can approximate the variance as follows:

$$\sigma \approx \frac{r}{\gamma} \sqrt{\frac{1 - \gamma^2}{-6 \ln \gamma}} \quad (7)$$

For the detailed calculations please refer to the supplements.

3D OOCS Encoder Blocks

We use Equation (2) to calculate the kernel weights for the On and Off (same equation, but with signs inverted) convolutions. Note that we only need to determine the kernel size, ratio of the radius of the center to surround, and sum of positive and negative values to compute the fixed kernels. Figure 3 shows the $5 \times 5 \times 5$ On kernel that we use in our experiments. Here we set $\gamma = \frac{2}{3}$ and $c = 3$.

For a given input χ , we calculate the On and Off responses by convolving χ with the computed kernels separately:

$$\begin{aligned} \chi_{\text{On}}[x, y, z] &= (\chi * +DoG[r, \gamma, c])[x, y, z] \\ \chi_{\text{Off}}[x, y, z] &= (\chi * -DoG[r, \gamma, c])[x, y, z] \end{aligned} \quad (8)$$

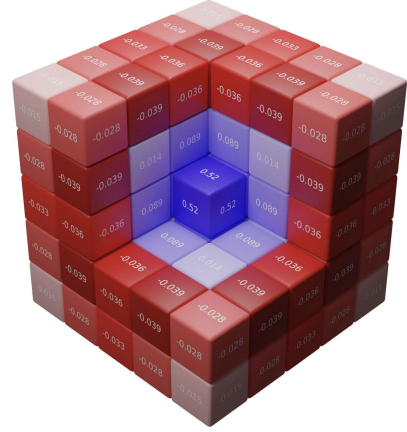


Figure 3: The 3D OOCS On kernel. The 3D OOCS Off kernel is complementary, that is, its signs are inverted.

Parameter	Lower bound	Upper bound	Default value
lr	10^{-6}	0.1	10^{-4}
β_1	0.1	0.9	0.9
dr	0.0	0.7	0.5

Table 1: Hyper-parameter ranges used in the optimal-configuration search for the baselines and their extension.

We extend a 3D U-Net-like segmentation network to a 3D OOCS network, by changing one of its primary encoder blocks, to a 3D OOCS encoder block, as shown in Figure 1. To this end, we first divide the convolution layers of the block into two parallel pathways, with half of the filters of the convolutions in the original layer, in each divided convolution, imitating the so-called On and Off pathways in the retina. We add the 3D On and Off convolved inputs of the block to the activation maps of the first convolution layers of the pathways. Finally, we concatenate the activation maps of the last layers on the pathways, resulting in the outputs with the same shapes as the outputs of the original block.

Experimental Evaluation

The proposed 3D OOCS filters are modular and independent of the network’s architecture. This allows them to be easily deployed to image segmentation tasks. All networks were evaluated on their ability to segment the prostate gland from MRIs. Owing to shape variability and poor tissue contrast in patient MRIs, prostate boundary delineation is challenging. The OOCS networks were compared against their respective counterparts by performing a rigorous robustness analysis.

U-Net-Like Networks

Along with the U-Net, we selected the Attention U-Net and the V-Net, as state-of-art U-Net benchmarks in the 3D medical image segmentation domain. These networks were selected based on the fact that they both introduced novel multi-view and multi-scale functions. These functions enhanced the receptive fields of the networks and reduced bottlenecks during computation, essentially shortening the

Model Name	DSC	HSD(mm)
U-Net	0.744 ± 0.24	33.777 ± 37.81
OOCS U-Net (k3)	0.798 ± 0.11	24.518 ± 12.46
OOCS U-Net (k5)	0.824 ± 0.07	24.474 ± 12.48
V-Net	0.792 ± 0.16	25.170 ± 22.91
OOCS V-Net (k3)	0.791 ± 0.13	26.488 ± 17.68
OOCS V-Net (k5)	0.825 ± 0.08	21.471 ± 10.01
Attention U-Net	0.824 ± 0.09	27.822 ± 14.64
OOCS Att. U-Net (k3)	0.845 ± 0.07	24.106 ± 14.70
OOCS Att. U-Net (k5)	0.835 ± 0.11	23.531 ± 14.89

Table 2: Segmentation test results of different U-Nets and their OOCS extensions.

time required to converge. Furthermore, the U-Net based architectures showed excellent performances in both the PROMISE-12 and the MSD datasets. These standard networks were extended with 3D-OOCS filters of two different kernel sizes: $k = 3$ and $k = 5$, respectively. The new networks are called OOCS U-Net (k3), OOCS U-Net (k5), OOCS Attention U-Net (k3), OOCS Attention U-Net (k5), OOCS V-Net (k3), and OOCS V-Net (k5), respectively.

Dataset and Pre-Processing

The PROMISE-2012 dataset offers 50 volumes of transversal T2-weighted MRIs of the prostate. In addition, the dataset is a compilation of scans obtained from multiple centers and vendors with different acquisition protocols. Due to this fact, there is a difference in the voxel-spacings and the slice thickness of the volumes. We tried to resample all scans to a uniform spacing, but this led to degradation of the MRIs. Therefore, we decided not to use the PROMISE-2012 dataset for our experiments.

On the other hand, the MSD-prostate dataset comprises of 48 (training =32, testing =16) multimodal (T2, ADC) 3D MRI samples. The scans were obtained from a single source and have a uniform voxel-spacing. However, the ground-truth labels for the testing images are not publicly available, and therefore, we used the 32 MRI volumes from the training set as our full dataset. The limited sample space posed the problem that the models would not be able to adapt to all the variations in the data. To overcome this drawback, we implemented a 5-fold cross-validation, where the complete dataset (n=32) was split into training (80%) and testing (20%) samples for each fold (for details, please refer to the supplements file). Since the T2-weighted volumes provide most of the necessary anatomical information, and the ADC modality is often used for tumour characterization/segmentation, we only considered the T2-weighted modality for our experiments. Furthermore, the ground-truth labels of the original dataset are separated into annotations of the central prostate gland and the peripheral zone. We combined the two target regions into one such that the networks could learn binary image segmentations. The MRI scans and the ground truth labels were resampled to (0.6, 0.6, 0.6) voxel spacings with tri-linear and nearest-neighbor interpolation techniques, respectively. The resampling was done to increase the slice thickness and facilitate the smooth functioning of the networks without any alteration in their original archi-

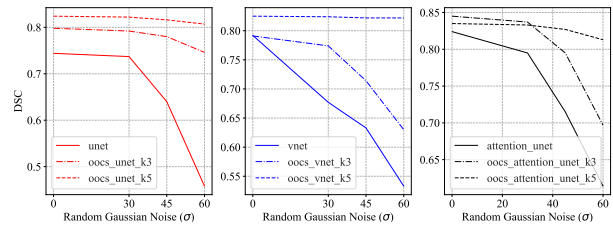


Figure 4: Dice-coefficient of the U-Net, V-Net, Attention U-Net, and their OOCS extensions, as a function of increasing input Gaussian noise variance. OOCS performs considerably more stable under Gaussian noise.

itecture. such that the networks could learn binary image segmentations. The MRI scans and the ground truth labels were resampled to (0.6, 0.6, 0.6) voxel spacings with tri-linear and nearest-neighbor interpolation techniques, respectively. The resampling was done to increase the slice thickness, and facilitate the smooth functioning of the networks, without any alteration in their original architecture.

Furthermore, the 3D images were cropped during the experiments to a selected shape of $160 \times 160 \times 64$ voxels per patch. Cropping ensured that the models were exposed to a majority of slices (in most cases, the complete portion) that contained the prostate gland in a single volume. For a given batch of samples, the intensity values of the MRIs were linearly scaled using a standard (z-score) normalization such that the mean value and standard deviation of the transformed data equaled 0 and 1, respectively. Since the dataset is made up of a small number of volumes, augmentation was performed to synthesize additional data using Torchio (Pérez-García, Sparks, and Ourselin 2021). The data pipeline carried out augmentations such as axial flips, elastic deformations, random crops, and affine transformations (scaling, rotation, and translation).

Implementation

A combination of two-loss functions: Binary Cross-Entropy loss (L_{BCE}) and Sørensen-Dice Loss (L_{dice}) (Sudre et al. 2017) called BCE-dice loss ($L_{BCE-dice}$) was used to train the models. This compound loss is defined over all semantic classes and is less sensitive to class imbalance as demonstrated experimentally in (Ma et al. 2021). The equations for BCE-dice loss are given as follows:

$$L_{BCE} = -\frac{1}{N} \cdot \sum_i^N g_i \cdot \log(p_i) + (1 - g_i) \cdot \log(1 - p_i)$$

$$L_{dice} = 1 - \frac{\sum_i^N p_i g_i + \epsilon}{\sum_i^N p_i + g_i + \epsilon} + \frac{\sum_i^N (1-p_i)(1-g_i) + \epsilon}{\sum_i^N 2-p_i-g_i + \epsilon} \quad (9)$$

$$L_{BCE-dice} = L_{BCE} + L_{dice}$$

N is the batch size, p_i and g_i are the predictions and ground-truth labels for a given batch respectively, and ϵ is 10^{-6} .

The models were evaluated based on two metrics: DSC and symmetric Hausdorff Distance (HSD). They were chosen because they exhibit low overall biases in 3D medical image segmentation tasks (Taha and Hanbury 2015).

We used the Adam optimization algorithm along with a cosine-annealing learning rate scheduler (Kingma and Ba

Model Name	$\sigma = 2$	$\sigma = 3$	$\sigma = 3.5$
U-Net	0.483 \pm 0.36	0.242 \pm 0.33	0.269 \pm 0.33
OOCS U-Net (k3)	0.378 \pm 0.36	0.311 \pm 0.37	0.257 \pm 0.34
OOCS U-Net (k5)	0.477 \pm 0.34	0.344 \pm 0.39	0.293 \pm 0.34
V-Net	0.489 \pm 0.38	0.243 \pm 0.35	0.365 \pm 0.37
OOCS V-Net (k3)	0.354 \pm 0.36	0.312 \pm 0.39	0.252 \pm 0.34
OOCS V-Net (k5)	0.461 \pm 0.37	0.341 \pm 0.40	0.264 \pm 0.36
Attention U-Net	0.688 \pm 0.23	0.503 \pm 0.28	0.533 \pm 0.28
OOCS Att. U-Net (k3)	0.691 \pm 0.16	0.467 \pm 0.35	0.427 \pm 0.34
OOCS Att. U-Net (k5)	0.773 \pm 0.11	0.535 \pm 0.33	0.528 \pm 0.32

Table 3: Robustness of U-Net variants against Gaussian Blur Noise (using DSC metric).

Model Name	$\sigma = 30$	$\sigma = 45$	$\sigma = 60$
U-Net	0.737 \pm 0.23	0.640 \pm 0.29	0.458 \pm 0.38
OOCS U-Net (k3)	0.792 \pm 0.12	0.780 \pm 0.13	0.746 \pm 0.18
OOCS U-Net (k5)	0.822 \pm 0.07	0.816 \pm 0.07	0.807 \pm 0.08
V-Net	0.677 \pm 0.30	0.633 \pm 0.30	0.533 \pm 0.34
OOCS V-Net (k3)	0.774 \pm 0.17	0.714 \pm 0.24	0.630 \pm 0.29
OOCS V-Net (k5)	0.824 \pm 0.08	0.822 \pm 0.08	0.822 \pm 0.09
Attention U-Net	0.795 \pm 0.15	0.715 \pm 0.26	0.614 \pm 0.32
OOCS Att. U-Net (k3)	0.837 \pm 0.08	0.795 \pm 0.13	0.697 \pm 0.25
OOCS Att. U-Net (k5)	0.833 \pm 0.11	0.827 \pm 0.12	0.813 \pm 0.13

Table 4: Robustness of U-Net variants against Random Gaussian Noise (using DSC metric).

Model Name	<i>transform#</i> = 5	<i>transform#</i> = 8	<i>transform#</i> = 10
U-Net	0.629 \pm 0.26	0.608 \pm 0.28	0.564 \pm 0.30
OOCS U-Net (k3)	0.484 \pm 0.24	0.451 \pm 0.32	0.506 \pm 0.31
OOCS U-Net (k5)	0.668 \pm 0.10	0.592 \pm 0.26	0.613 \pm 0.24
V-Net	0.619 \pm 0.30	0.674 \pm 0.26	0.591 \pm 0.32
OOCS V-Net (k3)	0.610 \pm 0.28	0.613 \pm 0.29	0.634 \pm 0.24
OOCS V-Net (k5)	0.757 \pm 0.08	0.669 \pm 0.26	0.659 \pm 0.23
Attention U-Net	0.764 \pm 0.14	0.806 \pm 0.09	0.775 \pm 0.12
OOCS Att. U-Net (k3)	0.788 \pm 0.07	0.821 \pm 0.07	0.770 \pm 0.11
OOCS Att. U-Net (k5)	0.771 \pm 0.10	0.800 \pm 0.09	0.747 \pm 0.15

Table 5: Robustness of U-Net variants against Motion Noise (using DSC metric).

2015; Loshchilov and Hutter 2017) throughout all the experiments. A batch normalization layer was placed after every convolution layer, to accelerate the speed of the experiments, and also serve as a regularizer (Ioffe and Szegedy 2015). All the networks were implemented in PyTorch (Paszke et al. 2019). We ran our experiments without data-parallelism on three NVIDIA Titan RTXs with 24 GB memory each. The gradient updates were evaluated with a batch size of two samples.

Training

Individual network hyper-parameter searches were done with MRIs of fold-1. This ensured that all models achieved their peak performance, and therefore, a fair and objective comparison was conducted among all networks.

The search space, as described in Table 1, was used to fine-tune the learning rate (lr), Adam’s momentum (β_1), and the dropout rate (dr), with the aid of the Hyperband technique and BOHB (Falkner, Klein, and Hutter 2018). Consequently, we performed the hyper-parameter search for nine models on the same 3D MRIs. The hyper-parameter search

executed 22 runs per network, of which 18 unique configurations were sampled. 14 of the 22 runs were evaluated at a maximum budget of 500 epochs, and the remaining were trained with a minimum budget of 166 epochs. Please see the supplements for the table of the tuned parameters found for each network.

After finding the optimal hyper-parameters for a network, four additional models of the same network were trained using the four remaining cross-validation folds, and the fine-tuned values of lr , β_1 and dr . This kind of training was repeated for all networks. In summary, we trained 45 separate models in total for 500 epochs apiece. The hyper-parameter search took, on average, approximately six days per network, while training experiments using the best parameters were completed in three days each.

Results

Testing The testing of the five individual models of the corresponding networks were also done using cross-validation. In the testing phase, initially, a window of shape $160 \times 160 \times 64$ is slid over the entire MRI scan of the

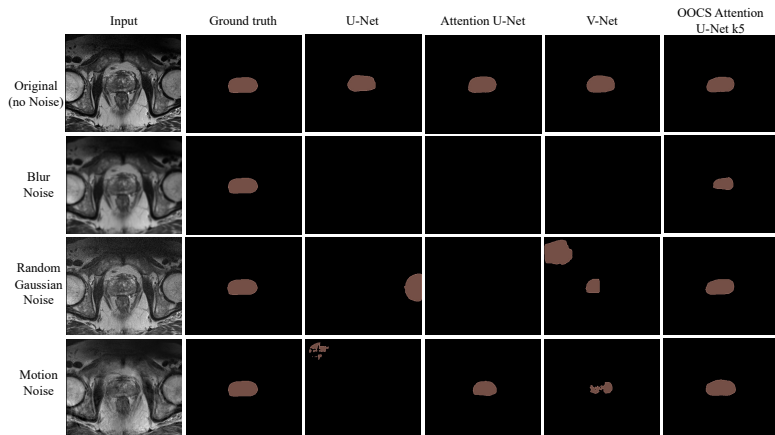


Figure 5: A qualitative comparison of the accuracy of the 3D OOCS-Attention-U-Net with k5 kernel, against the 3D U-Net, 3D Attention U-Net, and the 3D V-Net benchmark networks, on the prostate-gland segmentation task.

test sample with an overlap of $1/3$ in each dimension. The model makes inferences on every single normalized patch of the sliding window. This offers two advantages: First, the model’s ability to segment non-prostate volumes is determined. Second, by stitching the predicted labels together, the sliding window approach helps in computing the connected components of the resulting tensor.

The largest connected component of the prediction (apart from the background) is considered to contain the approximate prostate volume. A final patch of shape $160 \times 160 \times 64$, whose coordinates are determined by the centroid of the largest connected component, is again cropped from the 3D MRI and evaluated by the model. The testing process is carried out across all the 5-folds of a network. The average DSC and HSD of all the networks are listed in the Table 2. Here, it is evident that the OOCS-Attention-U-Net variations performed best. In addition to that, the OOCS extensions have consistently outperformed their original counterparts in most instances. The superior performance of the OOCS models showcases the ability of the inductive bias in the OOCS filters to delineate prostate contours effectively.

Robustness Evaluation To examine the robustness of the models, we introduced three types of noise: Gaussian blur, random Gaussian noise, and motion transform (simulating artifacts due to patient movement during acquisition), into the test volumes. We used the Torchio package, as mentioned earlier, to create noisy datasets. The steps described in the cross-validation testing stages were also employed to assess the performance of the models thoroughly.

Figure 5 illustrates a few of the examples with noise information, along with the predictions of the benchmark and the OOCS Attention U-Net (k5) models, respectively. Tables 3, 4 and 5 summarise the results of the robustness evaluation of the OOCS models and the state-of-the-art models.

In case of blurring, the average DSCs of the models decreased with the increase in standard deviation (σ) of the noise level. This behaviour was anticipated since higher deviations produced samples with large perturbations. On the other hand, the prostate predictions of the OOCS models

were considerably stable across both random Gaussian and motion artifacts. Figure 4 shows the significant robustness of OOCS networks against Gaussian noise. This demonstrates that the OOCS-extensions have a lower variance when compared to the benchmark networks on complex test sets. Finally, the OOCS-Attention-U-Net (k5) significantly outperforms all U-Net-like benchmarks and their extensions. However, the benchmark models occasionally yield better DSC scores than the OOCS-CNNs. This decline in the overall performance of the OOCS models is attributed to the presence of certain outliers.

Discussion

We expanded the On-Off center-surround retinal receptive fields to 3D kernels, and proposed a straightforward method to calculate the kernel weights. We designed OOCS encoder blocks using these fixed and pre-computed kernels as edge detection inductive biases, with On and Off parallel pathways similar to the ganglion pathways in the visual system. Our proposed 3D OOCS encoder block does not increase the number of training parameters of the networks and requires minimal computational overhead. Moreover, it is effortless to equip any UNet-like network with these encoder blocks. Our experiments on prostate segmentation tasks with our baseline networks and their OOCS extensions show notable enhancements in the performance of the OOCS-equipped networks, thus making 3D-OOCS a favorable method to achieve accurate results in 3D medical image segmentation tasks. Furthermore, our robustness experiments demonstrate the superior performance of OOCS extended networks. Robustness to distribution shifts is a crucial attribute of any deep neural network, and it is of even higher importance for networks used in critical domains like bio-medical tasks.

Future works This paper mainly focused on prostate segmentation from 3D MRIs. However, the use of 3D OOCS encoders in 3D U-Net-like models is not limited to this task. Therefore, we would like to apply them for segmenting other organs, from MRIs to other types of medical images too.

References

- AmericanCancerSociety. 2021. Key Statistics for Prostate Cancer - Prostate Cancer Facts. <https://www.cancer.org/cancer/prostate-cancer/about/key-statistics.html#written.by>. Accessed: 2021-08-06.
- Babaiee, Z.; Hasani, R.; Lechner, M.; Rus, D.; and Grosu, R. 2021. On-Off Center-Surround Receptive Fields for Accurate and Robust Image Classification. In Meila, M.; and Zhang, T., eds., *Proceedings of the 38th International Conference on Machine Learning*, volume 139 of *Proceedings of Machine Learning Research*, 478–489. PMLR.
- Brooks, R.; Hassabis, D.; Bray, D.; and Shashua, A. 2012. Turing centenary: Is the brain a good model for machine intelligence? *Nature*, 482: 462–3.
- Callaway, E. 2005. Structure and Function of Parallel Pathways in the Primate Early Visual System. *The Journal of Physiology*, 566(1): 13–19.
- Çiçek, Ö.; Abdulkadir, A.; Lienkamp, S. S.; Brox, T.; and Ronneberger, O. 2016. 3D U-Net: Learning Dense Volumetric Segmentation from Sparse Annotation. *CoRR*, abs/1606.06650.
- Dapello, J.; Marques, T.; Schrimpf, M.; Geiger, F.; Cox, D. D.; and DiCarlo, J. J. 2020. Simulating a Primary Visual Cortex at the Front of CNNs Improves Robustness to Image Perturbations. *bioRxiv*.
- Enroth-Cugell, C.; and Pinto, L. H. 1972. Properties of the Surround Response Mechanism of Cat Retinal Ganglion Cells and Centre-Surround Interaction. *The Journal of Physiology*, 220(2): 403–439.
- Falkner, S.; Klein, A.; and Hutter, F. 2018. BOHB: Robust and Efficient Hyperparameter Optimization at Scale. In *Proceedings of the 35th International Conference on Machine Learning*, 1436–1445.
- Gillespie, D.; Kendrick, C.; Boon, I.; Boon, C.; Rattay, T.; and Yap, M. H. 2020. Deep learning in magnetic resonance prostate segmentation: A review and a new perspective. arXiv:2011.07795.
- Goldenberg, S. L.; Nir, G.; and Salcudean, S. E. 2019. A new era: artificial intelligence and machine learning in prostate cancer. *Nature Reviews Urology*, 16(7): 391–403.
- Hassabis, D.; Kumaran, D.; Summerfield, C.; and Botvinick, M. 2017. Neuroscience-Inspired Artificial Intelligence. *Neuron*, 95(2): 245–258.
- Ioffe, S.; and Szegedy, C. 2015. Batch Normalization: Accelerating Deep Network Training by Reducing Internal Covariate Shift. *CoRR*, abs/1502.03167.
- Isensee, F.; Jaeger, P. F.; Kohl, S. A. A.; Petersen, J.; and Maier-Hein, K. H. 2021. nnU-Net: a self-configuring method for deep learning-based biomedical image segmentation. *Nature methods*, 18(2): 203–211.
- Isensee, F.; Petersen, J.; Klein, A.; Zimmerer, D.; Jaeger, P. F.; Kohl, S.; Wasserthal, J.; Köhler, G.; Norajitra, T.; Wirkert, S. J.; and Maier-Hein, K. H. 2019. nnU-Net: Self-adapting Framework for U-Net-Based Medical Image Segmentation. *CoRR*, abs/1809.10486.
- Kandel, E.; Jessell, T.; Schwartz, J.; Siegelbaum, S.; and Hudspeth, A. 2013. *Principles of Neural Science*. Fifth Edition. McGraw-Hill Medical / Education.
- Karimi, D.; Samei, G.; Kesch, C.; Nir, G.; and Salcudean, S. E. 2018. Prostate segmentation in MRI using a convolutional neural network architecture and training strategy based on statistical shape models. *International journal of computer assisted radiology and surgery*, 13(8): 1211–1219.
- Kingma, D. P.; and Ba, J. 2015. Adam: A Method for Stochastic Optimization. In Bengio, Y.; and LeCun, Y., eds., *3rd International Conference on Learning Representations, ICLR 2015, San Diego, CA, USA, May 7-9, 2015, Conference Track Proceedings*.
- Krizhevsky, A.; Sutskever, I.; and Hinton, G. E. 2012. ImageNet Classification with Deep Convolutional Neural Networks. In Pereira, F.; Burges, C. J. C.; Bottou, L.; and Weinberger, K. Q., eds., *Advances in Neural Information Processing Systems*, volume 25. Curran Associates, Inc.
- Kruzinga, P.; and Petkov, N. 2000. Computational Model of Dot-Pattern Selective Cells. *Biological Cybernetics*, 83(4): 313–325.
- Kuffler, S. 1953. Discharge Patterns and Functional Organization of MAMMALIAN RETINA. *Journal of Neurophysiology*, 16(1): 37–68.
- Lei, Y.; Dong, X.; Tian, Z.; Liu, Y.; Tian, S.; Wang, T.; Jiang, X.; Patel, P.; Jani, A. B.; Mao, H.; Curran, W. J.; Liu, T.; and Yang, X. 2020. CT prostate segmentation based on synthetic MRI-aided deep attention fully convolution network. *Medical Physics*, 47(2): 530–540.
- Li, Z.; Brendel, W.; Walker, E. Y.; Cobos, E.; Muhammad, T.; Reimer, J.; Bethge, M.; Sinz, F. H.; Pitkow, X.; and Tolia, A. S. 2019. Learning From Brains How to Regularize Machines. arXiv:1911.05072.
- Litjens, G.; Kooi, T.; Bejnordi, B. E.; Setio, A. A. A.; Ciompi, F.; Ghafoorian, M.; van der Laak, J. A.; van Ginneken, B.; and Sánchez, C. I. 2017. A survey on deep learning in medical image analysis. *Medical Image Analysis*, 42: 60–88.
- Litjens, G.; Toth, R.; (van de Ven), W.; Hoeks, C.; Kerkstra, S.; (van Ginneken), B.; Vincent, G.; Guillard, G.; Birbeck, N.; Zhang, J.; Strand, R.; Malmberg, F.; Ou, Y.; Davatzikos, C.; Kirschner, M.; Jung, F.; Yuan, J.; Qiu, W.; Gao, Q.; Edwards, P. E.; Maan, B.; van-der Heijden, F.; Ghose, S.; Mitra, J.; Dowling, J.; Barratt, D.; Huisman, H.; and Madabhushi, A. 2014. Evaluation of prostate segmentation algorithms for MRI: The PROMISE12 challenge. *Medical Image Analysis*, 18(2): 359–373.
- Loshchilov, I.; and Hutter, F. 2017. Fixing Weight Decay Regularization in Adam. *CoRR*, abs/1711.05101.
- Ma, J.; Chen, J.; Ng, M.; Huang, R.; Li, Y.; Li, C.; Yang, X.; and Martel, A. L. 2021. Loss odyssey in medical image segmentation. *Medical Image Analysis*, 71: 102035.
- Milletari, F.; Navab, N.; and Ahmadi, S. 2016. V-Net: Fully Convolutional Neural Networks for Volumetric Medical Image Segmentation. *CoRR*, abs/1606.04797.

- Nayebi, A.; and Ganguli, S. 2017. Biologically inspired protection of deep networks from adversarial attacks. arXiv:1703.09202.
- Oktay, O.; Schlemper, J.; Folgoc, L. L.; Lee, M. C. H.; Heinrich, M. P.; Misawa, K.; Mori, K.; McDonagh, S. G.; Hammerla, N. Y.; Kainz, B.; Glocker, B.; and Rueckert, D. 2018. Attention U-Net: Learning Where to Look for the Pancreas. *CoRR*, abs/1804.03999.
- Paszke, A.; Gross, S.; Massa, F.; Lerer, A.; Bradbury, J.; Chanan, G.; Killeen, T.; Lin, Z.; Gimelshein, N.; Antiga, L.; Desmaison, A.; Kopf, A.; Yang, E.; DeVito, Z.; Raison, M.; Tejani, A.; Chilamkurthy, S.; Steiner, B.; Fang, L.; Bai, J.; and Chintala, S. 2019. PyTorch: An Imperative Style, High-Performance Deep Learning Library. In Wallach, H.; Larochelle, H.; Beygelzimer, A.; d'Alché-Buc, F.; Fox, E.; and Garnett, R., eds., *Advances in Neural Information Processing Systems 32*, 8024–8035. Curran Associates, Inc.
- Petkov, N.; and Visser, W. 2005. Modifications of Center-Surround, Spot Detection and Dot-Pattern Selective Operators. Technical Report 2005-9-01, Institute of Mathematics and Computing Science, University of Groningen, Netherlands.
- Pérez-García, F.; Sparks, R.; and Ourselin, S. 2021. TorchIO: A Python library for efficient loading, preprocessing, augmentation and patch-based sampling of medical images in deep learning. *Computer Methods and Programs in Biomedicine*, 208: 106236.
- Rischke, H. C.; Nestle, U.; Fechter, T.; Doll, C.; Volegovaneher, N.; Henne, K.; Scholber, J.; Knippen, S.; Kirste, S.; Grosu, A. L.; and Jilg, C. A. 2013. 3 Tesla multiparametric MRI for GTV-definition of Dominant Intraprostatic Lesions in patients with Prostate Cancer—an interobserver variability study. *Radiat Oncol*, 8: 183.
- Rodieck, R. 1965. Quantitative Analysis of Cat Retinal Ganglion Cell Response to Visual Stimuli. *Vision Research*, 5(12): 583–601.
- Ronneberger, O.; Fischer, P.; and Brox, T. 2015. U-Net: Convolutional Networks for Biomedical Image Segmentation. In Navab, N.; Hornegger, J.; Wells, W. M.; and Frangi, A. F., eds., *Medical Image Computing and Computer-Assisted Intervention – MICCAI 2015*, 234–241. Cham: Springer International Publishing. ISBN 978-3-319-24574-4.
- Shapley, R.; and Perry, V. 1986. Cat and monkey retinal ganglion cells and their visual functional roles. *Trends in Neurosciences*, 9: 229 – 235.
- Simpson, A. L.; Antonelli, M.; Bakas, S.; Bilello, M.; Farhani, K.; van Ginneken, B.; Kopp-Schneider, A.; Landman, B. A.; Litjens, G.; Menze, B. H.; Ronneberger, O.; Summers, R. M.; Bilic, P.; Christ, P. F.; Do, R. K. G.; Gollub, M.; Golia-Pernicka, J.; Heckers, S.; Jarnagin, W. R.; McHugo, M.; Napel, S.; Vorontsov, E.; Maier-Hein, L.; and Cardoso, M. J. 2019. A large annotated medical image dataset for the development and evaluation of segmentation algorithms. *CoRR*, abs/1902.09063.
- Singh, S. P.; Wang, L.; Gupta, S.; Goli, H.; Padmanabhan, P.; and Gulyás, B. 2020. 3D Deep Learning on Medical Images: A Review. *Sensors*, 20(18).
- Spohn, S. K.; Bettermann, A. S.; Bamberg, F.; Benndorf, M.; Mix, M.; Nicolay, N. H.; Fechter, T.; Hölscher, T.; Grosu, R.; Chiti, A.; Grosu, A. L.; and Zamboglou, C. 2021. Radiomics in prostate cancer imaging for a personalized treatment approach - current aspects of methodology and a systematic review on validated studies. *Theranostics*, 11: 8027–8042.
- Steenbergen, P.; Haustermans, K.; Lerut, E.; Oyen, R.; De Wever, L.; Van den Bergh, L.; Kerkmeijer, L. G.; Pameijer, F. A.; Veldhuis, W. B.; van der Voort van Zyp, J. R.; Pos, F. J.; Heijmink, S. W.; Kalisvaart, R.; Teertstra, H. J.; Dinh, C. V.; Ghobadi, G.; and van der Heide, U. A. 2015. Prostate tumor delineation using multiparametric magnetic resonance imaging: Inter-observer variability and pathology validation. *Radiother Oncol*, 115(2): 186–190.
- Sudre, C. H.; Li, W.; Vercauteren, T.; Ourselin, S.; and Cardoso, M. J. 2017. Generalised Dice overlap as a deep learning loss function for highly unbalanced segmentations. *CoRR*, 10553: 240–248.
- Taha, A. A.; and Hanbury, A. 2015. Metrics for evaluating 3D medical image segmentation: analysis, selection, and tool. *BMC Medical Imaging*, 15(1): 29.
- Tian, Z.; Li, X.; Zheng, Y.; Chen, Z.; Shi, Z.; Liu, L.; and Fei, B. 2020. Graph-convolutional-network-based interactive prostate segmentation in MR images. *Medical Physics*, 47(9): 4164–4176.
- Tran, D.; Bourdev, L.; Fergus, R.; Torresani, L.; and Paluri, M. 2015. Learning Spatiotemporal Features with 3D Convolutional Networks. In *2015 IEEE International Conference on Computer Vision (ICCV)*, 4489–4497.
- Zaghloul, K.; Boahen, K.; and Demb, J. 2003. Different Circuits for ON and OFF Retinal Ganglion Cells Cause Different Contrast Sensitivities. *Journal of Neuroscience*, 23(7): 2645–2654.
- Zeng, Q.; Samei, G.; Karimi, D.; Kesch, C.; Mahdavi, S. S.; Abolmaesumi, P.; and Salcudean, S. E. 2018. Prostate segmentation in transrectal ultrasound using magnetic resonance imaging priors. *International journal of computer assisted radiology and surgery*, 13(6): 749–757.
- Zhou, Z.; Siddiquee, M. M. R.; Tajbakhsh, N.; and Liang, J. 2018. UNet++: A Nested U-Net Architecture for Medical Image Segmentation. *CoRR*, abs/1807.10165.